Journal of Electroceramics 4:2/3, 393–405, 2000
© 2000 Kluwer Academic Publishers. Manufactured in The Netherlands.

Oxide Thin Films for Tunable Microwave Devices

X.X. XI, HONG-CHENG LI,* WEIDONG SI, A.A. SIRENKO, I.A. AKIMOV,† J.R. FOX, A.M. CLARK & JIANHUA HAO

Department of Physics, The Pennsylvania State University, University Park, PA 16802

Abstract. Oxide thin films have been studied for frequency and phase agile electronics. The electric-field tuning of microwave devices employs ferroelectrics, while the Magnetic-field tuning uses ferrites. The critical material parameters for ferroelectric thin films are the tunability of the dielectric constant and the dielectric loss. This paper describes the current understanding of the fundamental mechanisms of these properties and the research efforts to improve them in ferroelectric thin films.

Keywords: ferroelectrics, ferrite, thin films, tunable microwave devices

1. Introduction

It is desirable for many microwave applications to tune the device characteristics. For example, planar microwave filters fabricated from thin film high temperature superconductors (HTS) have good frequency selectivity and low insertion loss, offering attractive options for commercial, military, and space-based communications [1]. However, it is difficult to meet the frequency specifications designed for the HTS microwave devices using the conventional design tools and lithography and processing techniques. Post-fabrication tuning of bandpass/bandreject frequencies is often required [2]. Another example is the phase shifter, which can be utilized for phased-array antennas that can be electronically steered [3]. If the cost of the such antenna is low, it could find applications in automobile collision warning, aircraft smart skin, etc. [4]. The tunable microwave devices have also been referred to as the frequency and phase agile electronics.

Tuning of the microwave devices can be achieved with both electric and magnetic field. The former employs the dielectric nonlinearity of the ferroelectrics (see Fig. 1(a), [5]) and the latter depends on the nonlinear magnetization of the ferrites (Fig. 1(b), [6]). When an electromagnetic wave travels in a medium of dielectric constant ε and magnetic susceptibility μ, its phase speed is $v_p = 1/\sqrt{\varepsilon\mu}$ and its intrinsic impedance is $Z = \sqrt{\mu/\varepsilon}$ [7]. In a microwave device, the electromagnetic wave travels in an environment of various media such as conductor, dielectric, air, etc. The phase speed and intrinsic impedance are now $v_p = 1/\sqrt{\varepsilon_{eff}\mu_{eff}}$ and $Z = \sqrt{\mu_{eff}\varepsilon_{eff}}$, respectively, where the effective ε_{eff} and μ_{eff} depend on the design of the devices and include to different degrees contributions from each media. When the media include a ferroelectric, applying an electric field will change its dielectric constant, hence ε_{eff}. When a ferrite is incorporated in the device, applying a magnetic field will change its magnetic susceptibility, hence μ_{eff}. The frequency and phase characteristics of the microwave device are thus tuned. Both electrically tuned [8–12] and magnetically tuned [6] microwave devices have been demonstrated. When both ferroelectric and ferrite are used, the frequency and phase properties and the impedance of the device can be tuned simultaneously by applying both electric and magnetic fields [13].

The desired properties of the tunable microwave devices are a large tunability and a low insertion loss.

*Permanent Address: National Lab for Superconductivity, Institute of Physics, Chinese Academy of Science, Beijing 100080, China.
†Permanent Address: A.F. Ioffe Physico-Technical Institute, Russian Academy of Sciences, St. Petersburg 194021, Russia.

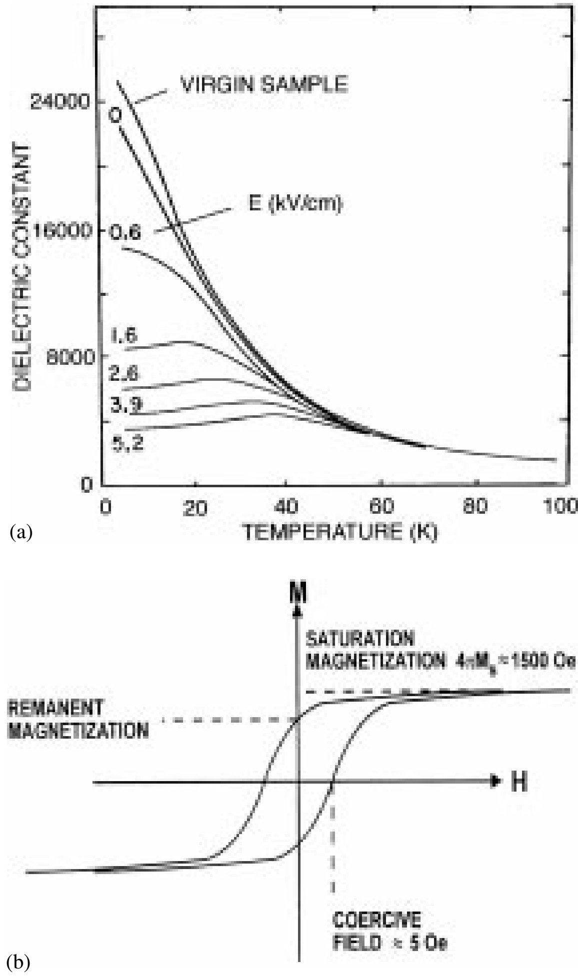

Fig. 1. (a) The dielectric constant of a single crystal STO versus temperature at different bias electric field (from Saifi and Cross [5]). (b) Hysteresis loop in the magnetization of ferrites.

To be able to compare the performances of difference devices, a figure of merit

$$K = 2\frac{\Delta f}{f} \cdot Q \quad (1)$$

has been used by many. For the frequency and phase agile materials, the critical parameters are a large dielectric nonlinearity and a low microwave loss. A similar figure of merit

$$K = \frac{\Delta \varepsilon}{\varepsilon \tan \delta_\varepsilon} \quad (2)$$

for ferroelectric, or

$$K = \frac{\Delta \mu}{\mu \tan \delta_\mu} \quad (3)$$

for ferrite have been used. The factor two in Eq. (1) arises from the fact that $2\Delta v_p = -\Delta\varepsilon$ or $2\Delta v_p = -\Delta\mu$.

Materials used for the frequency and phase agile microwave devices depend on the application. For the conductor, normal metals such as Au and Ag have been used for room temperature applications, and the high-T_c and low-T_c superconductors are desirable for high Q if the cryogenic requirements are acceptable. For electric-field tuning, the ferroelectrics of choice are $Ba_{1-x}Sr_xTiO_3$ (BST) for room temperature applications and $SrTiO_3$ (STO) for cryogenic applications. In both cases, the ferroelectrics are above the Curie temperature in the paraelectric phase. The Curie temperature of BST depends on the Ba/Sr ratio, and can be adjusted from 40 K for STO to 398 K for pure $BaTiO_3$. For magnetic-field tuning, ferrite yttrium iron garnet (YIG) substrates have been used to grow the low-T_c [14,15] and high-T_c [16,17] conducting lines. Devices made of these materials are expected to have small size and weight, low RF loss, continuous electronic variability, fast switching time and broad bandwidth. The cost will also be much lower than those of the current semiconductor or ferrite tunable devices. In the following, we will focused on the ferroelectric STO thin films, in particular the mechanisms of their different dielectric nonlinearity and loss properties as compared with the single crystal materials.

2. Incipient Ferroelectric Strontium Titanate

2.1. Lattice Dynamics and Quantum Fluctuations

In single crystal STO, there are two phase transitions driven by the ''soft modes'', the transverse optical phonons with low frequencies. One is the cubic-to-tetragonal (antiferrodistortive) phase transition at ~ 105 K, which is due to the instability of the zone-corner soft mode and involves the rotation of the Ti-O octahedral as shown in Fig. 2(a). The tetragonal structure is still centrosymmetric, hence the phase transition does not lead to ferroelectricity. The other phase transition should occur at ~ 40 K, which is due to the instability of the zone-center soft mode. The Ti ion would shift with respect to the oxygen ions, as shown in Fig. 2(b), giving rise to the spontaneous polarization and ferroelectricity.

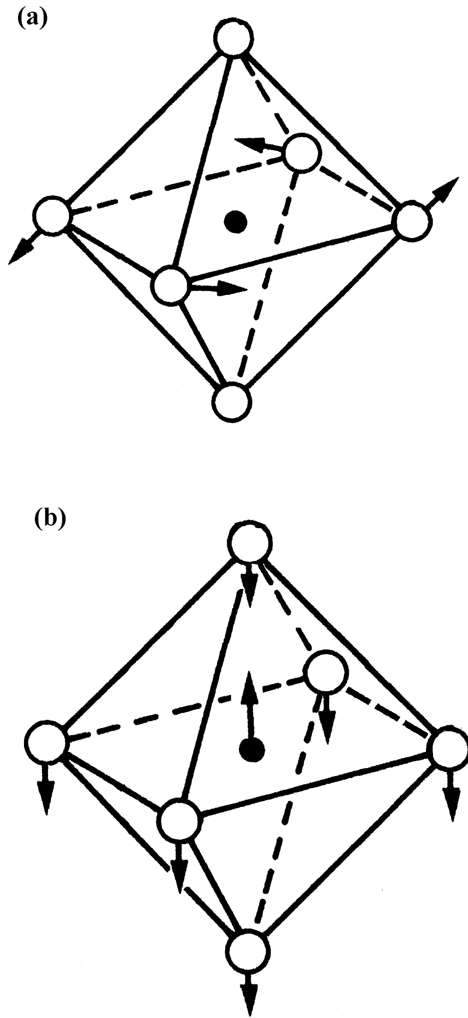

Fig. 2. Schematics of the two soft-mode-driven phase transitions in STO single crystals: (a) the cubic-to-tetragonal (antiferrodistortive) phase transition at $\sim 105\,\mathrm{K}$, and (b) the ferroelectric phase transition which would occur at $\sim 40\,\mathrm{K}$. The open circles are O ions and the solid circles are Ti ions.

According to the lattice dynamical theory,

$$\frac{\varepsilon}{\varepsilon_\infty} = \frac{\omega_{LO}^2}{\omega_{TO}^2} \tag{4}$$

(the Lyddane-Sachs-Teller (LST) relation), where ε_∞ is the optical frequency dielectric constant, and ω_{TO} and ω_{LO} the zone-center transverse and longitudinal optic mode frequencies. As shown in Fig. 3, the zone-center soft mode frequency of the STO single crystal goes to zero (instability) at $\sim 40\,\mathrm{K}$, however, the ferroelectric phase transition does not occur (there is no singularity in $1/\varepsilon$, which instead saturates at low temperatures) [18]. This is because the energy change associated with the ferroelectric phase transition is smaller than the energy of the quantum fluctuations, or the zero-point motion of the Ti ions [19]. In terms of the length scale, the shift of the Ti ion due to the ferroelectric phase transition should be 0.045 Å, which is smaller than its zero-point motion [19]. As a result, STO is an incipient ferroelectric, in which the ferroelectric phase transition is suppressed. The quantum mechanical effects in STO has been the subject of many theoretical and experimental studies [20], and Müller and Burkard first called STO a ''quantum paraelectric'' at low temperatures [19]. Recently, Müller et al. further proposed that the low temperature state of STO may be a coherent quantum state [21].

2.2. *Dielectric Nonlinearity and Loss*

The dielectric nonlinearity in STO arises from the hardening of the soft-mode phonon by electric field. In Fig. 4, the zone-center soft mode frequency as determined from the Raman scattering in an STO single crystal is shown as a function of temperature and electric field [22]: when an electric field is applied, the soft-mode frequency increases. According to the LST relation (Eq. (4)), a higher soft-mode frequency leads to a decrease in the low frequency dielectric constant. Indeed, the tunability in STO single crystals is consistent with the result of Fig. 4, and it diminishes above $\sim 80\,\mathrm{K}$ when the soft mode can no longer be hardened.

The intrinsic microwave loss in an ideal ferroelectric single crystal is related to the multiple-phonon absorption, in particular those involving the soft mode phonons [23]. In samples with defects [24], on the other hand, one-phonon absorption as well as phonon scattering on localized phonons near defects become possible, giving rise to extra losses. In addition to the defect-induced losses, in ferroelectric thin films, conductivity loss due to impurity and oxygen vacancies, uniform and local strain, and interfacial effects all contribute to loss. To reduce the loss while maintaining a large tunability is the objective of many active research.

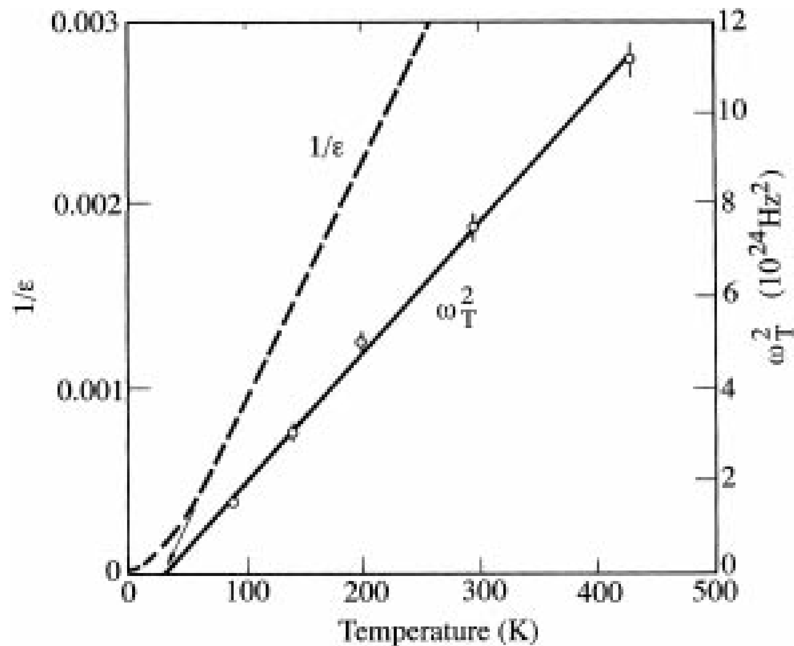

Fig. 3. The zone-center soft mode frequency and the reciprocal dielectric constant of an STO single crystal as a function of temperature. The soft mode frequency goes to zero at ~ 40 K, however, the ferroelectric phase transition does not occur (there is no singularity in $1/\varepsilon$) (from Cowley et al. [18]).

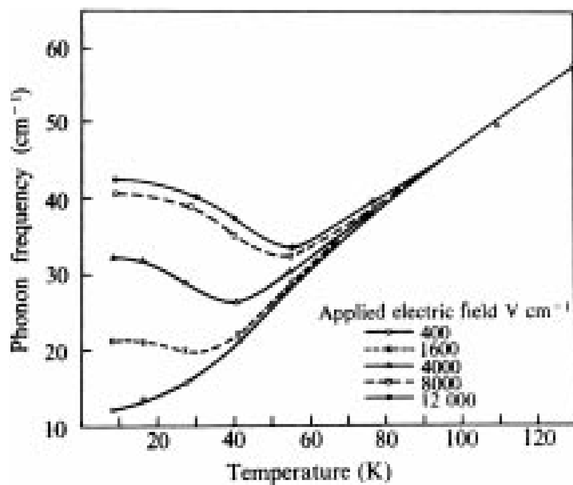

Fig. 4. The zone-center soft mode frequency as determined from the Raman scattering in an STO single crystal as a function of temperature and electric field (from Worlock et al. [22]).

3. Dielectric Properties of STO Thin Films

The dielectric properties of STO thin films are very different from those of STO single crystals. Figure 5 shows the dielectric constants, both real (ε') and imaginary (ε'') parts, for an STO single crystal [25] and a thin films as a function of temperature. The loss tangent, $\tan\delta = \varepsilon''/\varepsilon'$, is plotted as the inset. The ε' value is smaller in the thin film than in the single crystal due to the effects of the boundary condition [26], the interfacial dead layer [27–30], and/or the Schottky barriers at the film-electrode interfaces [31,32]. In contrast to the single crystal, in which ε' saturates below about 10 K, a broad peak exists at about 30 K in the thin film. The magnitude and the temperature dependence of ε'', in particular the existence of two peaks, are similar in both the single crystal and thin film, although the lower temperature peak appears at a higher temperature in the thin film. Because ε' is smaller, $\tan\delta$ is higher in the thin films.

To study the dielectric properties of STO thin films, we have used the pulsed laser deposition technique [33]. The typical deposition conditions are: excimer laser density 1–1.5 J/cm^2, substrate temperature 720–780°C, deposition rate Å/s, background vacuum 10_{-7}–10_{-6} Torr, oxygen pressure during the deposition 100 mTorr, and cooling of the deposited film in 500 Torr oxygen to room temperature. The schematic of the sample structure is shown in Fig. 6. Between the single crystal $LaAlO_3$ (LAO)

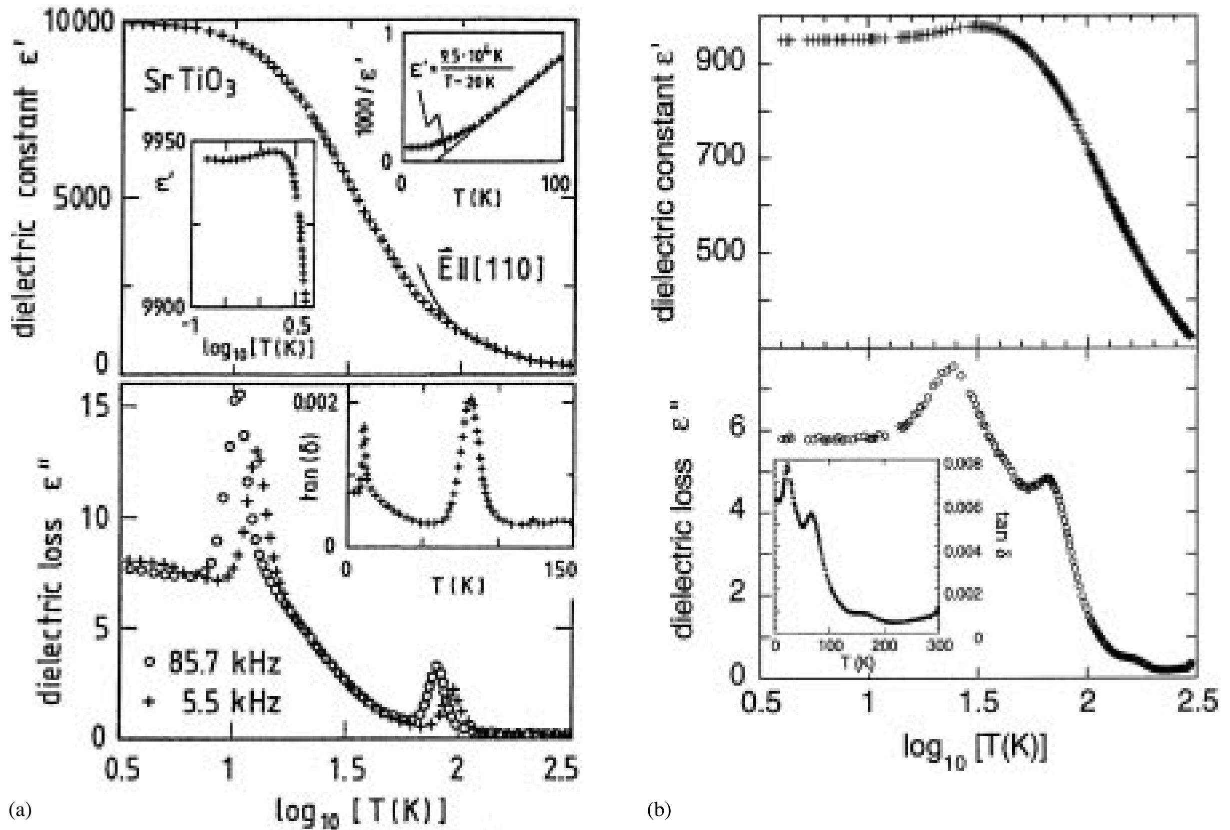

Fig. 5. The real (ε') and imaginary (ε'') parts of the dielectric constants for (a) an STO single crystal (from Viana et al. [25]) and (b) an STO thin films as a function of temperature.

($a = 3.793$ Å) substrate and the STO layer ($a = 3.905$ Å), a 0.35 μm metallic $SrRuO_3$ (SRO) film ($a = 3.93$ Å) is grown. The lattice constant mismatch between the STO and SRO layers is small (0.64%), and the relatively large SRO thickness is necessary to accommodate the difference between the lattice constants of LAO and STO. The STO film thickness ranges from 250 Å to 2.5 μm. X-ray diffraction measurement shows narrow full width at half maximum (FWHM) in both the Bragg peaks ($\sim 0.1°$) and the rocking curves ($\sim 0.16°$).

The low-frequency (50 Hz–1 MHz) dielectric measurements are carried out using a Hewlett-Packard 4284A Precision LCR Meter and/or a Keithley 3330 LCZ Meter. Great attention was paid to the accuracy of the dielectric loss measurement, which can be affected by the capacitance value, the measurement frequency and voltage level, the cable lengths, etc. and can vary widely. A four-terminal pair configuration with twisted coaxial cables extending all the way to the measured sample was used. The current and voltage contacts were geometrically arranged such that the effect of the contact resistance was minimized. For the capacitance values in our experiment, which ranged from several hundreds of pF to several nF, the measurement frequency of 1 kHz gave the smallest error of accuracy in tan δ of $\pm 8 \times 10^{-4}$.

3.1. Quantum Mechanical Behaviors

The STO thin films show very different quantum mechanical behaviors from those of single crystals. In STO single crystals, the saturation of ε' below about 10 K is characteristic of the quantum mechanical suppression of the ferroelectric ordering [19,25]. The appearance of the peak at about 30 K, although broad, signals the existence of ferroelectric order in the thin film. The hysteresis cycle in the polarization versus bias field measurement confirms some ferroelectric

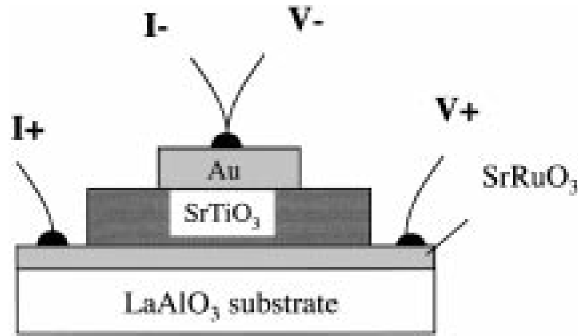

Fig. 6. Schematic of the sample structure. A conducting, lattice-matched SRO layer is used as the bottom electrode.

ordering in the thin film. This indicates that the quantum fluctuations are reduced in the thin films. (It is intriguing to notice that a much smaller maximum around 1–3 K has been observed in single crystals [34,25].)

The peaks in the imaginary part, ε'', also reveal the quantum mechanical behaviors of the thin films. For single crystals, the higher temperature (high-T) peak has been attributed to the $T = 105$ K antiferrodistortive phase transition, and the lower temperature (low-T) peak was suggested as an indication of a quantum phase transition into a coherent quantum state [25]. To study the relaxation dynamics in detail, we show Arrhenius plots for the two loss peaks in Fig. 7, where f is the measurement frequency and T_{peak} is the peak temperature in the ε''-T curve. The straight lines

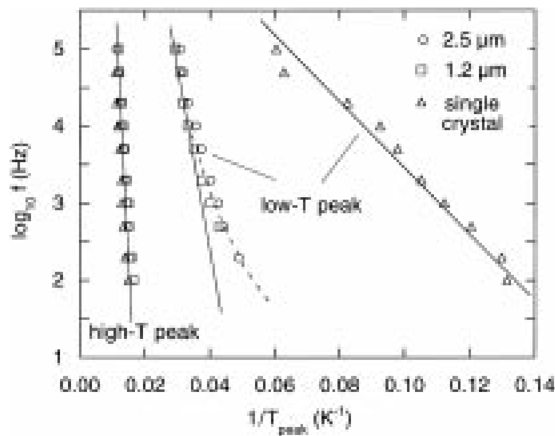

Fig. 7. Arrhenius plot for the high-T and low-T loss peaks for a 1.2 μm film, a 2.5 μm STO film, and a single crystal. f is the measurement frequency and T_{peak} is the peak temperature. The straight lines indicate thermally activated behaviors described by $f = f_0 \exp(-E/k_B T)$.

indicate thermally activated behaviors described by $f = f_0 \exp(-E/k_B T)$, where f_0 and E are hopping frequency and activation energy, respectively. The figure shows that the high-T peak data for the STO thin films overlap with that for the STO single crystal. In films with poor crystallinity, the high-T peak moves to much lower temperatures. The low-T peak, on the other hand, appears at much higher temperature in the thin films. Viana et al. reported a deviation from the thermally activated behavior in the single crystal at low temperatures and frequencies and explained it by quantum tunneling [25]. Such deviation was also observed in our thin films.

In theory, the phase transitions and critical phenomena in STO have been treated using the quantum Ising model in a transverse field with a Hamiltonian [20]

$$H = -J \sum_{\langle ij \rangle} \sigma_i^z \sigma_j^z - t \sum_i \sigma_i^x \tag{5}$$

where σ_i^x and σ_i^z are pseudospin operators related to the tunneling of Ti ion between four equivalent potential valleys for forming a Ti-O dipole bond, J is the ferroelectric coupling between different cells, and t is the tunneling strength. The relative strength J/t can be enhanced by applying uniaxial stress and electric field, both favor dipoles in a particular direction, thus suppressing quantum fluctuations [20]. The quantum mechanical behaviors of the STO films described above can be explained by the different J/t value as compared to that of single crystals due to strain induced by lattice mismatch and oxygen vacancies [35].

3.2. *Tunability and Loss*

The STO films showed large dielectric nonlinearity. Figure 8 shows the electric-field dependence of the dielectric constant and loss tangent for a 2.5 μm film at two different temperatures. At $T = 4.2$ K, the tunability is large, about 72%, but the loss is also large with a maximum $(\tan\delta)_{\text{MAX}} = 0.0036$. At $T = 190$ K, the tunability is smaller, only about 46%, but the loss is also smaller with $(\tan\delta)_{\text{MAX}} = 0.00094$. In Fig. 9, the percentage tuning versus temperature for the 2.5 μm STO film is plotted along with the result of an STO single crystal. The tunability of the STO film is about 70% at low temperatures, which decreases but persists to very high temperatures. For the single

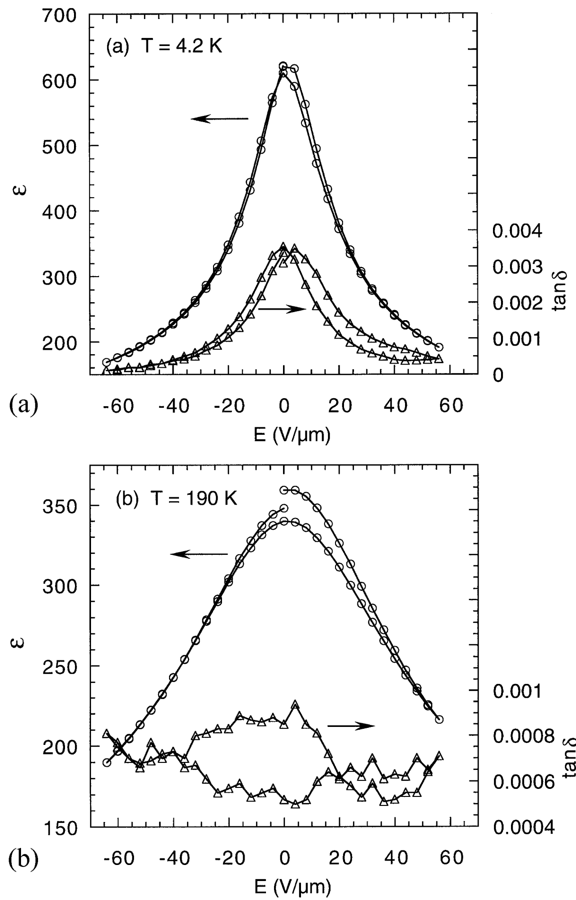

Fig. 8. Dielectric constant and loss tangent as a function of applied electric field for the 2.5 μm STO film measured at (a) $T = 4$ K and (b) $T = 190$ K.

crystal, on the other hand, the large tunability at low temperatures drops to near zero at about $T = 70$ K due to the diminishing electric-field hardening of the soft mode [36].

The K-factor as a function of temperature is plotted in Fig. 10 for the 2.5 μm STO film and the STO single crystal. Here, we use the maximum loss $(\tan\delta)_{\mathrm{MAX}}$ under all the applied fields to give a more conservative evaluation of the material quality. For the single crystal, the K-factor has a maximum of about 300 at low temperatures and drops to zero at about $T = 70$ K. For the thin film, the K-factor is about 200 at low temperatures and rises to more than 400 above $T = 100$ K. The result indicates that the STO thin films can be more useful than single crystals for tunable microwave devices if the operating temperature is to be above 70 K.

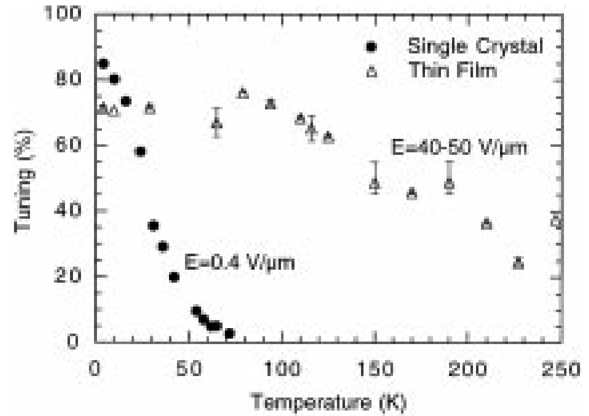

Fig. 9. Percentage tuning of the 2.5 μm STO film as a function of temperature. A single crystal data measured at 150 V (0.4 V/μm) is also included for comparison. The tunability of the STO film remains non-zero well after the single crystal tuning drops to zero.

3.3. Effects of Uniform Stress

In STO single crystals, the ferroelectric state has been induced by uniaxial stress [37], by bias field [38,39], and by impurity doping [40]. As mentioned earlier, these factors enhance the value of J/t and thus suppress the quantum fluctuations.

Experiments indicate that the appearance of ferroelectric order in STO thin films, as revealed by the broad peak in Fig. 5, is in part due to stress induced by the lattice mismatch between the STO film and the SRO layer. An important evidence comes from the lattice dynamics study using a metal-oxide bilayer Raman scattering (MOBRS) technique [41]. In this

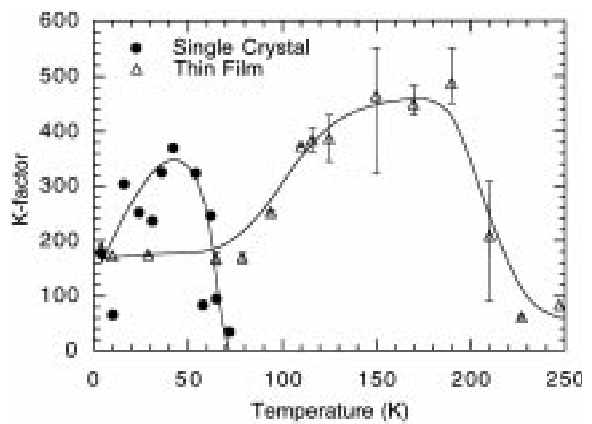

Fig. 10. The K-factor as a function of temperature for the 2.5 μm STO film and an STO single crystal. The STO thin film has higher K-factors above 70 K.

technique, a conducting metal oxide film (SRO in our case) is utilized as the light reflector (see Fig. 11(a)) so that the signal from the transparent STO film will not be overwhelmed by the substrate signals.

In Fig. 11(b), Raman spectra of STO films measured at $T = 5$ K are shown together with that of a single crystal. Bulk STO crystals have a centrosymmetric structure, and the zone-center optical phonons are of odd parity, and consequently not Raman active [42]. The Raman spectrum of the STO single crystal is characterized by the second-order scattering signal (the weak TO_2 and TO_4 peaks are likely due to the impurities). In the STO thin films, in contrast, strong peak due to the TO_2 (170 cm^{-1}), TO_3 (264 cm^{-1}), and TO_4 phonons (545 cm^{-1}) have been observed. These peaks can be observed up to room temperature. The appearance of the optical phonon peaks indicates a lowering of the crystal symmetry in the STO films. TO_3 is a silent non-polar phonon, which becomes Raman active only in the presence of a long-range lattice distortion of the order of phonon wavelengths [43].

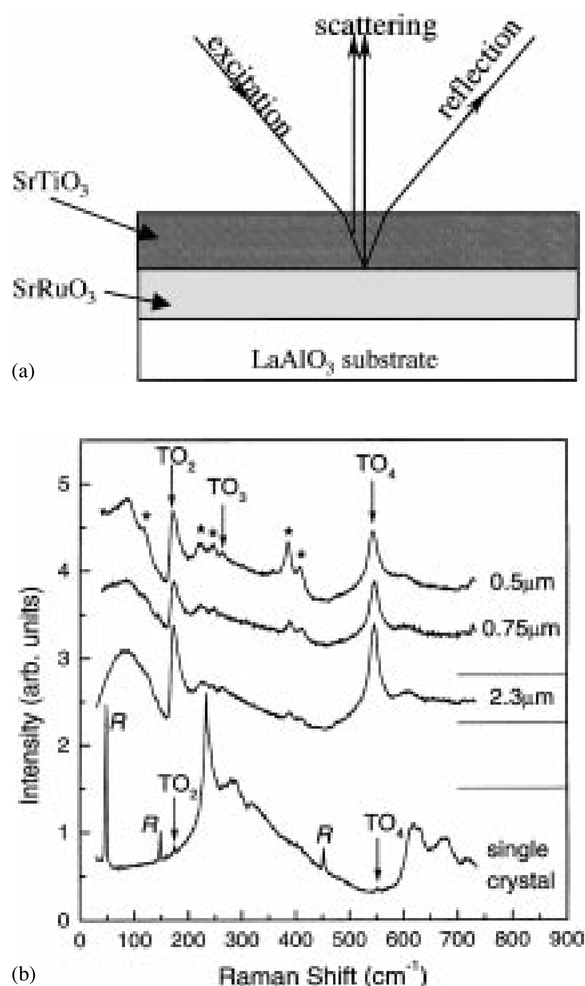

Fig. 11. (a) Schematic of the metal-oxide bilayer Raman scattering. The conducting layer reflects the laser beam so that it cannot reach the substrate, allowing the study of Raman scattering from the SrTiO3 thin film. (b) Raman spectra of STO films and a single crystal measured at $T = 5$ K. The stars denote the Raman lines related to the SRO buffer layer. Structural modes in bulk STO are marked with *R*. The arrows show positions of the zone center $TO_{2,3,4}$ phonons.

The uniform strain due to the lattice mismatch is further supported by the X-ray diffraction result, which shows that the structure of the STO films is tetragonal. The superlattice peak associated with the rotation of the Ti-O octahedral is observed at temperatures as high as 500 K [44]. Without stress, the structure of STO single crystal should be cubic at room temperature. The tetragonal phase is observed in films with thicknesses from 0.2–2.5 μm, suggesting that the effect of the lattice mismatch-induced strain extends to a large thickness. The persistence of the lattice mismatch-induced strain could be explained by the small mismatch between the STO film and the SRO layer (0.64%).

In Fig. 12, the thickness and electric-field dependence of the dielectric constant and loss tangent of the STO films are shown. At high temperatures above 100 K, $\tan\delta$ decreases by two orders of magnitude as the film thickness changes from 25 nm to 2.5 μm. A low loss of $\tan\delta = 6 \times 10^{-4}$ is obtained in the 2.5 μm film, which is close to the loss level found in STO single crystals. The two figures show remarkable similarities: the broad peak in ε moves to higher temperature and the low-T loss peak is depressed when the film thickness decreases and when an electric field is applied. Both the lattice mismatch-induced stress, which decreases as the film thickness increases, and the electric field enhance ferroelectric coupling J/t, hence suppress the quantum fluctuations.

To reduce the effect of stress due to lattice mismatch, various approaches have been pursued. The buffer layers of better lattice match have been used, such as SRO in our work. The lattice matched insulator Sr_2AlTaO_6 is being investigated for microwave frequency applications. Jia et al. [45] has used an LAO homoepitaxial interlayer on the LAO substrate and found that the quality factor of the

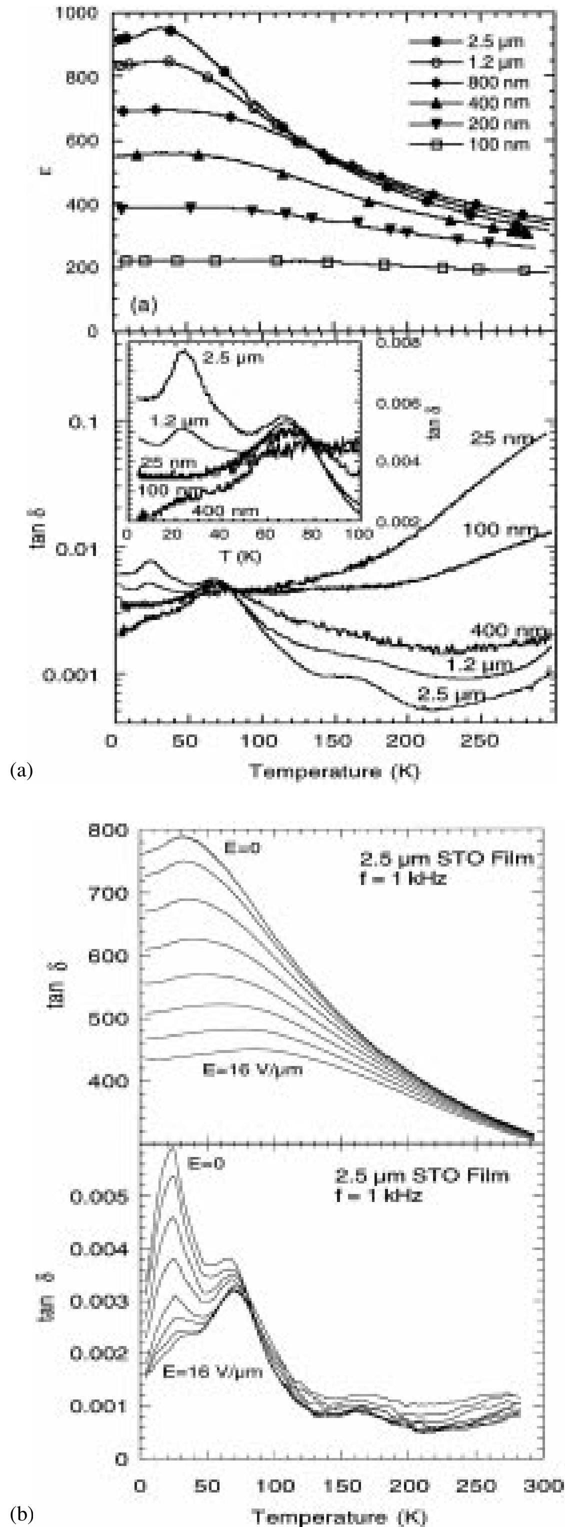

Fig. 12. (a) Thickness and (b) electric-field dependence of the dielectric constant and loss tangent of STO thin films.

microwave device is improved by more than 50%. Cross-sectional TEM shows that this layer has many defects, which may act to reduce the stress when STO grows epitaxially on the LAO substrate. Epitaxial lift-off using sacrificial layers has been applied by Eddy et al. [46] and Dalberth et al. [47,48] in high T_c $YBa_2Cu_3O_7$ (YBCO)/STO bilayer, in which YBCO is the sacrificial layer. Epitaxial lift-off using Crystal Ion Slicing has also been investigated, in which selective etching of ion implanted single crystal separates the top layer of 9 μm from the bulk single crystal [49].

3.4. Effects of Oxygen Vacancies

The local lattice distortions in the STO films also contribute to the lowering of the crystal symmetry. It has been established that micro polar regions exist in doped STO and $KTaO_3$ single crystals [50,51], oxygen vacancy is the main defect structure in perovskite titanates [52], and oxygen vacancies could become dipole centers [53,54]. In Fig. 13, the Raman line shape of the polar TO_2 peak is shown for a 2.3 μm STO film. It is strongly asymmetric: the scattering intensity increases at the high-energy side and is depressed at the low-energy side. The dashed line is a fit using the Fano profile [55]:

$$I(\omega) = A\frac{(q + E(\omega))^2}{1 + E(\omega)^2} \tag{6}$$

where $E(\omega) = 2(\omega - \omega_0)/\Gamma$. Here ω_0 is the phonon frequency in the absence of interaction, Γ is its

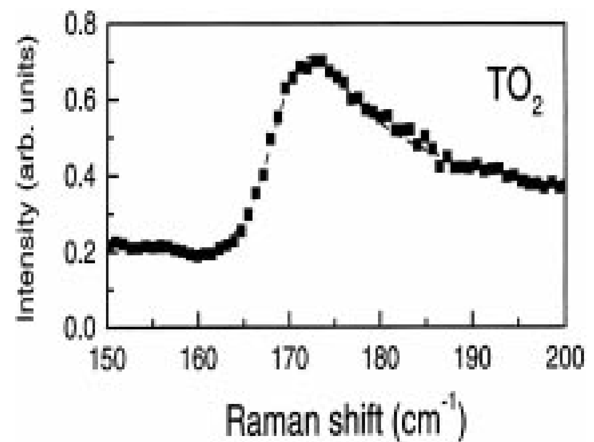

Fig. 13. The Fano-like TO_2 peak for a 2.3 μm STO film at $T = 5$ K. The dashed line represents the fit to the Fano profile.

FWHM, A is the amplitude, and q is the asymmetry parameter, which is found to be positive in our spectra. The Fano profile indicates an interference between the polar optical phonon with a continuum, which is likely the polarization fluctuations in micro polar regions induced by the oxygen vacancies. The micro polar region by nature implies non-uniformity, which is proved by the X-ray diffraction result that the superlattice peak associated with the tetragonal phase is very broad ($\sim 0.1°$) [44]. The diffused peak observed in the ε'-T curves in such films [33] also points to the non-uniform dielectric properties in the STO thin films.

It is impossible to rule out the existence of impurities: even in samples of highest purity, acceptor-type impurities have been detected [56]. The defect chemistry studies show, however, that the existence of these impurities, as well as cation off-stoichiometry, often results in oxygen vacancies in the titanates [56]. In thin films, besides cation off-stoichiometry and acceptor-type impurities, oxygen vacancies can also result from insufficient oxygenation during the deposition process. It is difficult to precisely determine the oxygen content in a thin film. Using luminescence and optical second-harmonic generation measurements, Fischer et al. determined that the density of the dipolar micro-regions surrounding the oxygen vacancies is about $10^{17}\,\mathrm{cm}^{-3}$ in well oxidized $KTaO_3$ single crystals [57]. The STO thin films in this work are highly resistive (resistivity is higher than $10^{13}\,\Omega\mathrm{cm}$), which indicates a low free-carrier density. We can thus give a rough estimate of the oxygen vacancy density in the STO films to be of the order of $10^{17}\,\mathrm{cm}^{-3}$.

The Fano asymmetry does not vanish in the entire temperature region measured, indicating that the micro polar regions exist in the STO films even at room temperature. This explains the existence of the dielectric nonlinearity in STO films up to room temperature whereas in single crystals, the nonlinearity (related to the hardening of the soft modes) vanishes above 70 K.

Various approaches to reduce oxygen vacancies in the ferroelectric thin films have been investigated. The Naval Research Laboratory group has studied post deposition annealing in oxygen and has observed lower loss and larger tuning in the BST films after the annealing. It is also being studied to use more active oxygenates, such as ozone, oxygen plasma, etc. during the deposition and cooling. Doping has been shown to neutralize free charges or to pin ionic motion. This has been investigated by Horwitz et al. by using targets of various doping for thin film deposition and by Chang et al. using combinatorial synthesis [58]. The effects of oxygen vacancies in ferroelectric perovskite have also been studied through first-principles calculation [59].

3.5. Interfacial Effects

Interfaces between the ferroelectric thin films and the electrodes affect the measured dielectric properties. It has been proposed that the reduction of ε in ferroelectric thin films can be explained by the existence of interfacial ''dead layer'' at one or both electrodes with poor dielectric properties [28,29]. They may arise from the oxygen interdiffusion, chemical reaction, structural defects, or Schottky barriers at the interfaces. Treating the dead layer as a capacitance, C_i, in series with bulk film capacitance, C_b, the measured capacitance may be expressed as

$$\frac{1}{C} = \frac{1}{C_b} + \frac{1}{C_i} \tag{7}$$

or

$$\frac{t}{\varepsilon} = \frac{t - 2t_i}{\varepsilon_b} + \frac{2t_i}{\varepsilon_i} \tag{8}$$

where t is the total film thickness, t_i is the interfacial layer thickness (assuming that the interfacial layers at both electrodes have the same properties), ε_b is the film ''bulk'' dielectric constant and ε_i is the interfacial layer dielectric constant. Assuming $t_i \ll t$, one can plot $1/\varepsilon$ vs $1/t$ and obtain $2t_i/\varepsilon_i$ from the slope of the linear fit. Such a fit is demonstrated in the inset to Fig. 14. Subtracting the contribution of the interfacial dead layer, the ε vs T curves for STO thin films of different thickness collapse together, confirming the significance of the dead layer effect. One can in principle extend the series-connected capacitor model to the dielectric loss by replacing ε with $\varepsilon' + i\varepsilon''$ in the above procedure. However, such exercise has been not successful. The dielectric loss of the dead layer increases as the film thickness decreases.

It is intriguing to examine the result in Fig. 15, which shows the tunability of the 2.5 μm STO film and STO single crystal measured at 1 kHz at $T = 4.2$ K. When the applied field on the thin film is scaled by

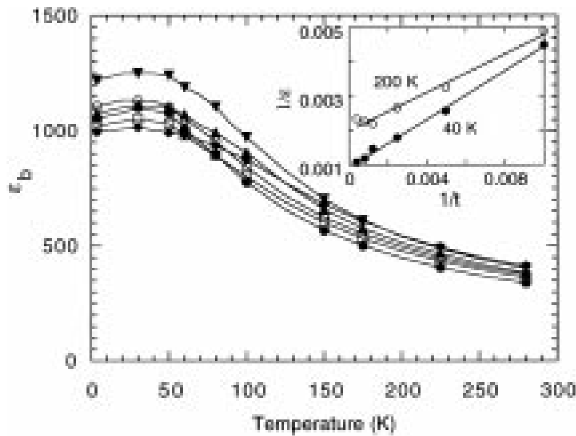

Fig. 14. The film ''bulk'' dielectric constant as obtained by correcting the result of Fig. 12(a) for the interfacial dead layer effect using a series-connected capacitor model. The inset shows the $1/\varepsilon$ vs. $1/t$ curves at two temperatures used to obtain $2t_i/\varepsilon_i$ from the linear fit.

over 200 times, the normalized $\varepsilon/\varepsilon(0)$ versus E curves overlap with that of the single crystal, in which the effect of the interface layer is less important. This may have some bearing on the effect of the film/electrode interface layer. In Fig. 16, the leakage current in a Au/

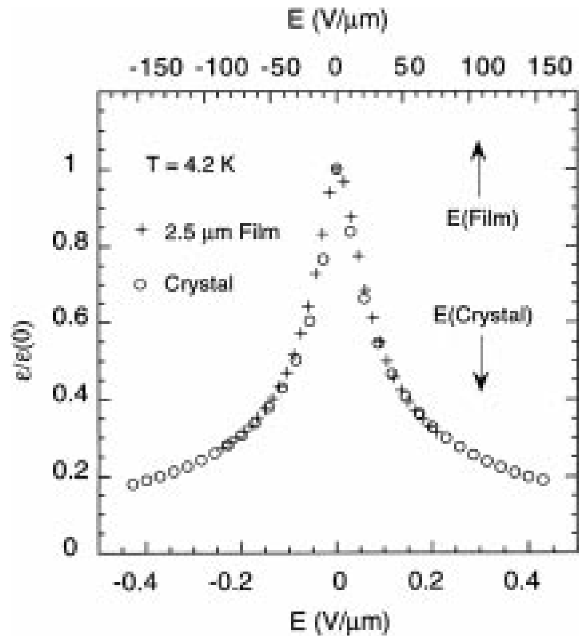

Fig. 15. The electric field dependence of the normalized dielectric constant of a 2.5 μm STO film and an STO single crystal measured at 1 kHz at $T = 4.2$ K. When the applied field on the thin film is scaled by over 200 times, the two curves overlap.

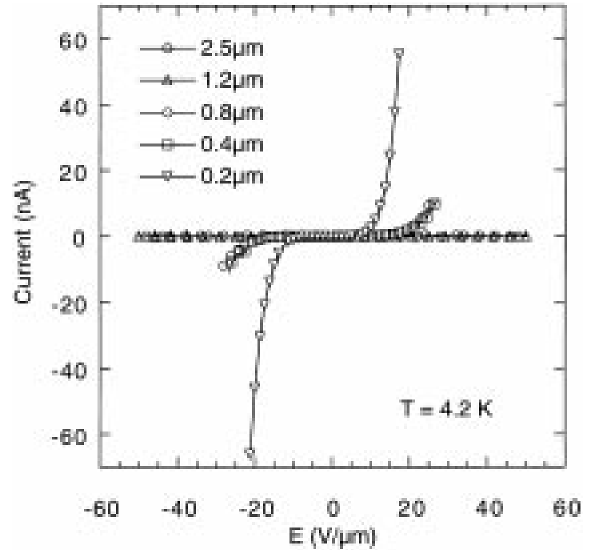

Fig. 16. The leakage current in a Au/STO/SRO structure for STO films of different thickness as a function of electric field. The breakdown field for the thinner films is smaller than that for the thicker films.

STO/SRO structure for STO films of different thickness is shown as a function of electric field. The breakdown field for the thinner films is smaller than that for the thicker films. Although shorts due to particles on the film surface cannot be ruled out, the result may be an indication of the not well developed Schottky barriers in thinner films as compared to the well developed Schottky barriers in thicker films.

The effect of Schottky barriers on the measured dielectric properties of ferroelectric films is of particular interest. The conventional techniques to measure the Schottky barrier height, including the $C-V$ measurement, are complicated by the voltage dependence of the dielectric constant [60], which in thin films exist even at room temperature. The photoemission technique used by Copel et al. to measure the band bending due to metallization on STO and BST [61] can be very useful for this purpose. Changing electrode materials with different work functions does not seem to affect the measured dielectric loss of STO thin films. Besides changing the electrode materials, Takeuchi et al. have doped the ferroelectric films, which modifies the energy gap of the ferroelectric, hence affecting the Schottky barrier characteristics [62]. Treatment of STO surface with ozone annealing has been reported to improve the interface properties [63].

4. Other Activities on Tunable Microwave Devices

There are other activities aimed at achieving tunable microwave devices. These include exploring frequency agile materials other than STO, such as the pyrochlore compounds, tungsten bronze structure ferroelectrics, etc. as well as the Ruddlesdon-Popper type layered compounds $Sr_{n+1}Ti_nO_{3n+1}$ by the Ferroelectric Resource Center for Frequency Agile Materials for Electronics at Penn State University; developing characterization techniques for frequency agile materials such as the Evanescent Microwave Microscopy by Gao et al. [64], the Confocal Scanning Optical Microscopy (CSOM) and the Apertureless Near-Field Scanning Optical Microscopy (ANSOM) by Hubert and Levy et al. [65], and various microwave characterization techniques designed for low loss ferroelectric materials [66,67]; using micro-electromechanical systems (MEMS) for variable capacitors, active antennas etc.; and the study of film growth kinetics using techniques such as the *in situ* real-time ion-beam analysis by Auciello et al. [68] and the Oblique-Incidence Reflectance Difference Spectroscopy (OI-RDS) by Zhu et al. [69,70].

5. Summary

Frequency and phase agile microwave devices have wide range of applications. Ferroelectric and ferrite materials are used for electric and magnetic field tuned devices, respectively. The major materials challenge is to reduce loss in thin films while maintaining a large tunability. For the incipient ferroelectric STO, uniform and local stress, oxygen vacancies, and interfacial effects have been identified as factors affecting the quantum mechanical behaviors, the dielectric nonlinearity, and the dielectric loss in the thin films.

Acknowledgment

Helpful discussions with M. W. Cole, E. Tosatti, David Vanderbilt, D. G. Schlom, L. E. Cross, A. S. Bhalla, C. A. Randall, S. Trolier-McKinstry, V. Belitsky, H. Vogt, J. Levy, C. B. Eom, and V. C. Matijasevic are gratefully acknowledged. This work is partially supported by NSF under Grant Nos. DMR-9623889, DMR-9623315, and DMR-9702632, by the NRL SPAWAR program, by DOE under Grant No. DFFG02-84ER45095, and by DARPA FAME program.

References

1. T. Van Duzer, *IEEE Trans. Appl. Supercond.*, **7**, 98 (1997).
2. F.A. Miranda, C.H. Mueller, G.A. Koepf, and R.M. Yandrofski, *Supercond. Sci. Technol.*, **8**, 755 (1995).
3. C.M. Jackson, J.H. Kobayashi, A. Lee, C. Pettiette-Hall, and J.F. Burch, *Microw. Opt. Techn. Lett.*, **5**, 722 (1992).
4. V.K. Varadan, V.V. Varadan, K.A. Jose, and J.F. Kelly, *Smart Mater. Struct.*, **3**, 470 (1994).
5. M.A. Saifi and L.E. Cross, *Phys. Rev. B*, **123**, 2 (1970).
6. G.F. Dionne and D.E. Oates, *IEEE trans. Magn.*, **33**, 3421 (1997).
7. A.R. von Hippel, *Dielectrics and Waves* (Artech House, Boston, 1995).
8. A.T. Findikoglu, Q.X. Jia, X.D. Wu, G.J. Chen, T. Venkatesan, and D. Reagor, *Appl. Phys. Lett.*, **68**, 1651 (1996).
9. R.S. Kwok, S.J. Fiedziuszko, F.A. Miranda, G.V. Leon, M.S. Demo, and D.Y. Bohman, *IEEE Trans. Appl. Supercond.*, **7**, 3706 (1997).
10. G. Subramanyam, F.V. Keuls, and F.A. Miranda, *Microwave and Guided Wave Lett.*, **8**, 78 (1988).
11. F.W. Van Keuls, R.R. Romanofsky, D.Y. Bohman, M.D. Winters, F.A. Miranda, C.H. Mueller, R.E. Treece, T.V. Rivkin, and D. Galt, *Appl. Phys. Lett*, **71**, 3075 (1997).
12. S.W. Kirchoefer, J.M. Pond, A.C. Carter, W. Chang, K.K. Agarwal, J.S. Horwitz, and D.B. Chrisey, *Microw. Opt. Techn. Lett.*, **18**, 168 (1998).
13. H. Jiang, *private communications.*
14. G.F. Dionne, D.E. Oates, D.H. Temme, and J.A. Weiss, *IEEE trans. Microw. Theory Tech.*, **44**, 1361 (1996).
15. D.E. Oates and G.F. Dionne, *IEEE MTT-S Inter. Microw. Symp. Digest*, **1**, 303 (1997).
16. A. Piqué, K.S. Harshavardhan, J. Moses, M. Mathur, E. Belohoubek, T. Venkatesan, E.J. Denlinger, D. Kalokitis, A. Fathy, V. Pendrick, M. Rajeswari, and W. Jiang, *Appl. Phys. Lett.*, **67**, 1778 (1995).
17. Q.X. Jia, A.T. Findikoglu, P. Arendt, S.R. Foltyn, J.M. Roper, J.R. Groves, J.Y. Coulter, Y.Q. Li, and G.F. Dionne, *Appl. Phys. Lett*, **72**, 1763 (1998).
18. R.A. Cowley, *Phys. Rev. Lett*, **9**, 159 (1962).
19. K.A. Müller and H. Burkard, *Phys. Rev. B*, **19**, 3593 (1979).
20. E. Tosatti and R. Martoňák, *Solid State Commun.*, **92**, 167 (1994).
21. K.A. Müller, W. Berlinger, and E. Tosatti, *Z. Phys. B*, **92**, 277 (1991).
22. J.M. Worlock and P.A. Fleury, *Phys. Rev. Lett.*, **19**, 1176 (1967).
23. A.K. Tagantsev, in *Ferroelectric Ceramices* N. Setter and E.L. Colla, eds., **127** (Birkhäuser, Basel, 1993).
24. V.L. Gurevich and A.K. Tagantsev, *Adv. Phys.*, **40**, 719 (1991).
25. R. Viana, P. Lunkenheimer, J. Hemberger, R. Böhmer, and A. Loidl, *Phys. Rev. B*, **50**, 601 (1994).
26. O.G. Vendik and L.T. Ter-Martirosyan, *Sov. Phys.-Solid State*, **36**, 1778 (1994).

27. K. Abe and S. Komatsu, *Jap. J. of Appl. Phys.*, **32**, L1157 (1993).
28. C. Zhou and D.M. Newns, *J. Appl. Phys.*, **82**, 3081 (1997).
29. C. Basceri, S.K. Streiffer, A.I. Kingon, and R. Waser, *J. Appl. Phys.*, **82**, 2497 (1997).
30. H.C. Li, W. Si, A.D. West, and X.X. Xi, *Appl. Phys. Lett.*, **73**, 464 (1998).
31. G.W. Dietz, W. Antpöhler, M. Klee, and R. Waser, *J. Appl. Phys.*, **78**, 6113 (1995).
32. G.W. Dietz and R. Waser, *Thin Solid Films*, **299**, 53 (1997).
33. H.C. Li, W. Si, A.D. West, and X.X. Xi, *Appl. Phys. Lett.*, **73**, 190 (1998).
34. E. Fischer and E. Hegenbarth, *Ferroelectrics Lett.*, **5**, 21 (1985).
35. X.X. Xi, H. Li, W. Si, and A.A. Sirenko, unpublished.
36. J.L. Servoin, Y, Luspin, and F. Gervis, *Phys. Rev. B*, **22**, 5501 (1980).
37. H. Uwe and T. Sakodo, *Phys. Rev. B*, **13**, 271 (1976).
38. J. Hemberger, P. Lunkenheimer, R. Viana, R. Böhmer, and A. Loidl, *J. Phys.: Condens. Matter*, **8**, 4673 (1996).
39. D.E. Grupp and A.M. Goldman, *Phys. Rev. Lett.*, **78**, 3511 (1997).
40. J.G. Bednorz and K.A. Müller, *Phys. Rev. B*, **52**, 2289 (1984).
41. V.I. Merkulov, J.R. Fox, H. Li, W. Si, A.A. Sirenko, and X.X. Xi, *Appl. Phys. Lett.*, **72**, 3291 (1998).
42. W.G. Nilsen and J.G. Skinner, *J. Chem. Phys.*, **48**, 2240 (1968).
43. S.K. Manlief and H.Y. Fan, *Phys. Rev. B*, **5**, 4046 (1972).
44. B.O. Wells, M.V. Zimmerman, H. Nakao, S.M. Shapiro, A.M. Clark, and X.X. Xi, unpublished (1998).
45. Q.X. Jia, A.T. Findikoglu, D. Reagor, and P. Lu, *Appl. Phys. Lett.*, **73**, 897 (1998).
46. M.M. Eddy, R. Hanson, M.R. Rao, and B. Zuck, *Mater. Res. Soc. Symp. Proc.*, **474**, 365 (1997).
47. M.J. Dalberth, R.E. Stauber, J.C. Price, C.T. Rogers, and D. Galt, *Appl. Phys. Lett.*, **72**, 507 (1998).
48. M.J. Dalberth, J.C. Price, and C.T. Rogers, *Mater. Res. Soc. Symp. Proc.*, **493**, 371 (1998).
49. M. Levy, R.M. Osgood, Jr., R. Liu, L.E. Cross, G.S. Cargill III, A. Kumar, and H. Bakhru, *Appl. Phys. Lett.*, **73**, 2293 (1993).
50. U. Bianchi, W. Kleemann, and J.G. Bednorz, *J. Phys.: Condens. Matter*, **6**, 1229 (1994).
51. J. Toulouse, P. DiAntonio, B.E. Vugmeister, X.M. Wang, and L.A. Knaus, *Phys. Rev. Lett.*, **68**, 232 (1992).
52. R. Waser, in *Ferroelectric Ceramics* N. Setter and E.L. Colla, eds., **273** (Birkhäuser, Basel, 1993).
53. H. Uwe, H. Yamaguchi, and T. Sakodo, *Ferrolectrics*, **96**, 123 (1989).
54. S.A. Prosandeyev and I.A. Osipenko, *Phys. Stat. Sol. (b)*, **192**, 37 (1995).
55. U. Fano, *Phys. Rev.*, **124**, 1866 (1961).
56. R. Waser and D.M. Smyth, in *Ferroelectric thin films: synthesis and basic properties* C.P. de Araujo, J.F. Scott, and G.W. Taylor, eds., p. 47 (Gordon and Breach Publishers, Amsterdam, 1996).
57. C. Fischer, C. Auf Der Horst, P. Voigt, S. Kapphan, and J. Zhao, *Radiat. Eff. and Defects in Solids*, **136**, 85 (1995).
58. H. Chang, C. Gao, I. Takeuchi, Y. Yoo, J. Wang, P.G. Schultz, X.-D. Xiang, R.P. Sharma, M. Downes, and T. Venkatesan, *Appl. Phys. Lett.*, **72**, 2185 (1998).
59. C.H. Park and D.J. Chadi, *Phys. Rev. B*, **57**, R13961 (1998).
60. T. Shimizu and H. Okushi, to appear in *Phys. Rev. B* (1999).
61. M. Copel, P.R. Duncombe, D.A. Neumayer, T.M. Shaw, and R.M. Tromp, *Appl. Phys. Lett.*, **70**, 3227 (1997).
62. I. Takeuchi, H. Chang, C. Gao, P.G. Schultz, X. Xiang, R.P. Sharma, M. Downes, and T. Venkatesan, *Appl. Phys. Lett.*, **73**, 894 (1995).
63. T. Shimizu and H. Okushi, *Appl. Phys. Lett.*, **67**, 1411 (1995).
64. C. Gao, F. Duewer, Y. Lu, and X.-D. Xiang, *Appl. Phys. Lett.*, **73**, 1146 (1993).
65. C. Hubert and J. Levy, *Appl. Phys. Lett.*, **73**, 3229 (1998).
66. J. Krupka, R.G. Gayer, M. Kuhn, and J.H. Hinken, *IEEE Trans. Microw. Theory Tech.*, **42**, 1886 (1994).
67. J. Baker-Jarvis, R.G. Geyer, J.H. Grosvenor, and M.D. Janezic, *Phys. Rev. Lett.*, **5**, 571 (1998).
68. O. Auciello, A.R. Krauss, J. Im, D.M. Gruen, E.A. Irene R.P.H. Change, and G.E. McGuire, *Appl. Phys. Lett.*, **69**, 2671 (1996).
69. X.D. Zhu, H.B. Lu, G.-Z. Yang, Z.-Y. Li, B.-Y. Gu, and D.-Z. Zhang, *Phys. Rev. B*, **57**, 2514 (1998).
70. X.D. Zhu, unpublished.